Sustainable Carbon Materials

https://doi.org/10.48130/scm-0026-0021

Original Research

Open Access

Iron and phosphoric acid co-modified fishbone char for olefin-rich bio-oil production from waste agricultural films via microwave-assisted pyrolysis

Jie Yang[1,2,3,4#], Yue Zhang[3,4#], Dengle Duan[2,5], Xun Chen[3,4], Xiaoyan Lan[3,4], Lu Gan[3,4], Leilei Dai[6], Yunpu Wang[7], Roger Ruan[8], Erguang Huo[9], Rongge Zou[10], Lianfu Zhang[1*], Jian Zhang[3,4*] and Yunfeng Zhao[3,4*]

Received: 3 February 2026

Revised: 5 March 2026

Accepted: 19 April 2026

Published online: 30 June 2026

Abstract

Microwave-assisted catalytic pyrolysis offers an efficient route for converting waste plastics into liquid fuels, addressing both petroleum resource scarcity and environmental pollution. However, achieving high oil yields and targeted product selectivity requires careful optimization of catalyst design and operating conditions. In this work, a series of acid–metal bifunctional catalysts was synthesized via phosphoric acid modification and iron loading, and their effects on plastic pyrolysis behavior were systematically investigated. Among them, 20Fe–30P@FC exhibited outstanding catalytic performance, delivering a bio-oil yield as high as 89.32 wt.%. The resulting bio-oil was dominated by olefins (84.03%), with minor fractions of alkenes (8.98%) and aromatics (4.80%). Further catalyst screening over a wide range of phosphoric acid contents (0 wt.%–40 wt.%) and iron loadings (0 wt.%–30 wt.%) confirmed the superior performance of 20Fe–30P@FC in terms of both oil yield and product distribution. Process optimization revealed that the highest bio-oil yield and optimal oil quality were achieved at a pyrolysis temperature of 550 °C, a catalytic temperature of 350 °C, and a catalyst-to-feedstock ratio of 1:2. Regeneration experiments demonstrated stable catalytic activity over multiple cycles, indicating the robustness of 20Fe–30P@FC for microwave-assisted catalytic pyrolysis of plastic mulch. Overall, this study presents a viable strategy for the targeted catalytic conversion and high-value utilization of waste plastics, including ground film plastics.

Keywords: Microwave-assisted pyrolysis, Acid–metal bifunctional catalyst (20Fe-30P@FC), Ground film plastics, Olefin selectivity

Highlights

- A high-performance acid-metal bifunctional catalyst (20Fe–30P@FC) was developed for microwave-catalyzed pyrolysis.
- This catalyst achieved a bio-oil yield as high as 89.32 wt.% with outstanding olefin selectivity (84.03%).
- Optimal process parameters were determined: pyrolysis temperature of 550 °C, catalytic temperature of 350 °C, and catalyst-to-feedstock ratio of 1:2.
- The catalyst demonstrated stable activity after multiple regeneration cycles, exhibiting practical application potential for processing waste plastics such as agricultural plastic mulch.

# Authors contributed equally: Jie Yang and Yue Zhang

* Correspondence: Lianfu Zhang (lianfu@jiangnan.edu.cn); Jian Zhang (zhangjian0411@163.com); Yunfeng Zhao (yunfeng_zhao@shzu.edu.cn)

Full list of author information is available at the end of the article.

https://doi.org/10.48130/scm-0026-0021

Graphical abstract

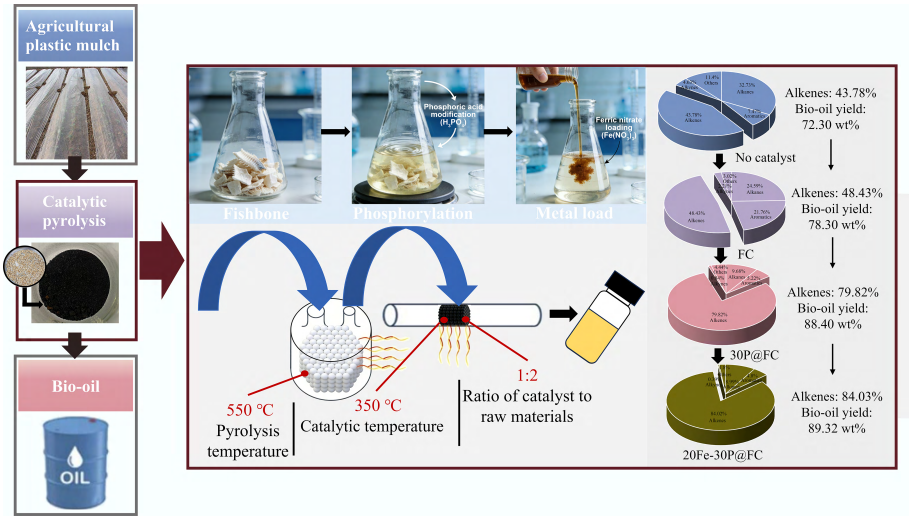

Introduction

Low-density polyethylene (LDPE) mulch film is widely used in modern agriculture due to its ability to increase soil temperature, retain moisture, suppress weeds, and improve crop yield and quality[1]. However, its large-scale application has led to increasing energy consumption and persistent environmental pollution[1]. Conventional disposal methods, including landfilling and incineration, fail to recover carbon-based energy and often generate microplastics and toxic emissions, thereby aggravating ecological degradation[2,3]. Because LDPE consists primarily of carbon and hydrogen without heteroatoms, it represents an attractive feedstock for producing value-added products such as carbon nanotubes[4], naphtha[5], aviation fuel[6], and gasoline[7] via thermochemical conversion.

Pyrolysis has emerged as a promising chemical recycling route for converting waste LDPE into liquid hydrocarbons, contributing to circular carbon utilization while mitigating greenhouse gas emissions[8]. Nevertheless, non-catalytic pyrolysis typically requires high operating temperatures, consumes substantial energy, and exhibits poor product selectivity. For example, Hegedüs et al.[9] reported low aromatic selectivity in LDPE pyrolysis oils at temperatures of 525–650 °C in the absence of catalysts. Similarly, olefin selectivity of only 33.68% has been observed, accompanied by the formation of long-chain hydrocarbons that are unfavorable for fuel applications[10]. These limitations highlight the necessity of efficient catalysts to promote C–C scission and enhance short-chain olefin production.

Recently, biomass-derived catalyst supports have attracted increasing interest due to their sustainability and low cost. Bone char (BC), produced by pyrolyzing animal bones, possesses a hierarchical porous structure and a unique organic–inorganic composition[11]. Global meat processing generates substantial bone waste, which is projected to reach 45 million tons by 2027[12,13], yet much of this resource remains underutilized. Bone char consists of nano-hydroxyapatite (60 wt.%–85 wt.%) and nitrogen-doped amorphous carbon (15 wt.%–40 wt.%), providing favorable mechanical strength, thermal stability, and metal anchoring capability[11]. These properties make BC a promising catalyst support. However, pristine BC exhibits limited intrinsic activity, necessitating surface modification to tailor acidity and active sites for selective catalytic conversion.

Acid treatment is an effective strategy for enhancing catalytic performance. Phosphoric acid (H_3PO_4) modification introduces stable phosphorus-containing functional groups and generates both Brønsted and Lewis acid sites on carbonaceous supports[14]. These acid sites facilitate β-scission of carbocation intermediates while suppressing excessive hydrogenation and coke formation, thereby improving olefin selectivity[15,16]. In addition, phosphorus species can regulate the electronic structure of supported metals and strengthen metal–support interactions, enhancing catalyst stability[17]. Despite extensive studies on acidic catalysts for plastic pyrolysis[18,19], achieving high liquid yields with controllable olefin selectivity at low cost remains challenging.

Loading transition metals provides an additional pathway to improve catalytic efficiency. Iron (Fe), an abundant and inexpensive metal, effectively promotes C–C bond cleavage and hydrogen transfer during polymer cracking[20,21]. Dong et al.[22] demonstrated enhanced catalytic cracking performance using Fe-loaded shark bone biochar. Although Fe-supported carbon materials and bone char have been explored for plastic pyrolysis[20,23], the coupled effects of phosphoric acid pre-modification and subsequent Fe loading on bone char supports have not been systematically investigated. Moreover, the degree of acid treatment strongly influences the physicochemical properties of the support, which in turn governs catalytic behavior[10,24]. Understanding this synergy is therefore essential.

Microwave-assisted pyrolysis (MAP) offers further opportunities for process intensification by enabling rapid, volumetric, and selective heating[25–28]. Compared with conventional conductive heating, MAP minimizes temperature gradients and significantly accelerates reaction kinetics[29–31]. Optimization of operating parameters, including temperature and catalyst-to-feedstock ratio, can markedly improve liquid yield and product quality[32–36]. For instance, Fan et al.[37] achieved a jet fuel yield of 98.78 wt.% from polystyrene using MAP, while Zhou et al.[38] reported an energy efficiency of 89.6% in a continuous microwave pyrolysis system. Despite these advances, selectively producing high-quality olefin-rich bio-oil (C_6–C_{12}) through catalyst design within MAP systems remains a key challenge.

In this study, a dual-functional fish bone-derived catalyst is developed via phosphoric acid modification followed by iron loading and applied to the microwave-assisted catalytic pyrolysis of LDPE mulch film. The effects of acid concentration and Fe loading on catalytic performance are systematically evaluated. Key process parameters, including pyrolysis temperature, catalytic temperature, and catalyst-to-feedstock ratio, are optimized to maximize bio-oil yield and light olefin selectivity. Catalyst regeneration is also examined. This work provides insights into the rational design of low-cost, efficient, and stable catalysts for microwave-assisted plastic valorization and offers a practical strategy for the directional conversion of waste plastics into high-value hydrocarbons.

Materials and methods

Feedstock and characterization

The experimental feedstock consisted of whitefish bones (*Coregonus peled*) obtained from the Xinjiang Sayram Lake Fishery Technology Development Co., Ltd (Xinjiang, China), and low-density polyethylene (LDPE) mulch film purchased from the Hebei Weipai Technology Co., Ltd (Hebei, China). The pretreatment methods for both feedstocks followed those described in our previous study[35]. The LDPE mulch film was characterized by elemental analysis, proximate analysis (Supplementary Table S1), and thermogravimetric analysis (TGA) (Supplementary Fig. S1). Ferric nitrate nonahydrate ($Fe(NO_3)_3{\cdot}9H_2O$; purity 98.5%) and phosphoric acid (H_3PO_4; purity 99.9%) were purchased from the Shanghai Macklin Biochemical Technology Co., Ltd (Shanghai, China).

Preparation of catalyst

The production and pretreatment of the fish bone-based catalyst were described in our previous work[10]. Briefly, the pretreated fish bones were immersed in 100 mL of phosphoric acid solution with varying concentrations (0 wt.%, 10 wt.%, 20 wt.%, 30 wt.%, 40 wt.%) and stirred for 12 h at 600 rpm. The solids were then rinsed with deionized water until the pH of the rinse water reached approximately 5, followed by drying in an oven. The dried mass was weighed, and an aqueous metal precursor solution was prepared according to the target iron loading (0 wt.%, 10 wt.%, 20 wt.%, 30 wt.%). The dried phosphoric acid-treated bones were subsequently immersed in the metal solution and stirred for 24 h. After solid-liquid separation, the material was dried at 100 °C for 6 h. The catalyst precursor was finally carbonized in a microwave digestion system at 600 °C for 40 min with a power of 800 W under a nitrogen atmosphere to obtain the final catalyst. The catalysts are denoted based on their nominal iron loading and phosphoric acid concentration, e.g., 20Fe-30P@FC.

For regeneration tests, the spent 20Fe-30P@FC catalyst was calcined in the microwave digestion system using an identical heating program (600 °C, 40 min, N_2 atmosphere). The regenerated catalyst was then reused in the catalytic pyrolysis experiment. This regeneration cycle was repeated five times to evaluate the catalyst's stability and reusability.

Experimental setup and conditions

A two-stage fixed-bed reactor system, as illustrated in Supplementary Fig. S2 and consistent with our prior setup for plastic pyrolysis and catalytic cracking[10], was employed in this study. The system comprised several sections: a gas supply unit, a quartz tube reactor divided into two independently controlled temperature zones (an upper pyrolysis zone and a lower catalytic zone), a condenser system, and a gas collection unit.

Prior to each experiment, a specified mass of the catalyst was placed in a quartz boat and positioned in the catalytic zone, while a predetermined mass of LDPE feedstock was placed in another quartz boat in the pyrolysis zone. The catalyst-to-feedstock mass ratios investigated were 0:1, 1:3, 1:2, 1:1, 2:1, and 3:1. The reactor was purged with nitrogen at a flow rate of 100 mL min^{-1} for 15 min to establish an inert atmosphere. Subsequently, the pyrolysis temperature (450, 500, 550, 600, or 650 °C) and the catalytic temperature (300, 350, 400, 450, or 500 °C) were set. Pyrolysis was conducted for 40 min with a microwave power of 800 W. During the reaction, the nitrogen flow rate was maintained at 30 mL min^{-1}. The evolved vapors passed through the catalyst bed and were then condensed in a series of condensers cooled with an ice-water mixture. The non-condensable gases were collected in a 1 L Tedlar gas sampling bag from the start of the pyrolysis process.

Methods of analysis and characterization

All experiments were performed in triplicate to ensure reproducibility. The yields of pyrolysis products were calculated as follows:

$$\text{Bio}-\text{Oil yield (wt.\%)} = \frac{m_L}{m} \times 100\% \quad (1)$$

$$\text{Bio}-\text{Char yield (wt.\%)} = \frac{m_S}{m} \times 100\% \quad (2)$$

$$\text{Coke yield (wt.\%)} = \frac{\mathrm{m_C}}{\mathrm{m}} \times 100\% \quad (3)$$

$$\text{Gas yield (wt.\%)} = 100\% - \text{Bio} - \text{oilyield} - \text{Bio} - \text{char yield} - \text{Coke yield} \quad (4)$$

where, m_L denotes the mass of bio-oil, m_s denotes the mass of biocarbon, m_c denotes the mass of tar, m_g denotes the mass of gas, and m denotes the mass of feedstock.

The selectivity (S) for specific compounds (such as alkanes, aromatics, olefins, and alkynes) is calculated as follows:

$$\mathrm{S}_i\ (\%) = \frac{P_i}{\sum P_i} \times 100\% \quad (5)$$

where, S denotes selectivity, i represents selectivity for alkanes, aromatics, alkenes, alkynes, others, Less C_6, C_6–C_{12}, C_{13}–C_{16}, etc., P is the total peak area for a specific substance, and ∑Pa is the total peak area.

Gas chromatography-mass spectrometry (GC-MS) was employed for gas component analysis. Specific parameters are detailed in Supplementary Section 1.

N_2 adsorption-desorption isotherms were measured at –196 °C using a Micromeritics ASAP 2460 analyzer. Prior to analysis, samples were degassed at 120 °C for 12 h. The specific surface area was calculated using the Brunauer-Emmett-Teller (BET) method, and the pore volume was determined by the Barrett-Joyner-Halenda (BJH) method from the adsorption branch. Thermal stability was assessed by thermogravimetric-differential thermal analysis (TG-DTA) on a Mettler TGA/DSC1 instrument (Switzerland) under an air atmosphere. X-ray photoelectron spectroscopy (XPS) analysis was performed on a Thermo Fisher Scientific Nexsa G2 spectrometer (USA) with an Al Kα X-ray source (hv = 1,486.6 eV). Survey and high-resolution spectra were collected with pass energies of 100 and 20 eV, respectively, and step sizes of 1.0 and 0.05 eV. The actual iron content in the catalysts was quantified by inductively coupled plasma optical emission spectrometry (ICP-OES) on an Agilent 5110 instrument (USA). Functional groups were characterized by Fourier-transform infrared spectroscopy (FT-IR) using a Thermo Scientific Nicolet iS20 spectrometer (USA) in the range of 400–4,000 cm^{-1}. The surface acidity was evaluated by ammonia temperature-programmed desorption (NH_3-TPD) on a BelCatII instrument (Japan). Approximately

https://doi.org/10.48130/scm-0026-0021

100 mg of catalyst was pretreated in helium (He) at 400 °C for 1 h, cooled to 100 °C, and then exposed to a 15% NH_3/He mixture (50 mL min^{-1}) for 2 h. After purging with He to remove physisorbed NH_3, the temperature was ramped to 800 °C at 10 °C min^{-1} under He flow, and the desorbed NH_3 was monitored by a thermal conductivity detector (TCD). Hydrogen temperature-programmed reduction (H_2-TPR) was conducted on a Thermo Scientific TPDRO 1100 system equipped with a TCD. About 30 mg of fresh catalyst was pretreated in Ar at 300 °C for 1 h, cooled to 50 °C, and then heated to 900 °C at 10 °C min^{-1} under a 5% H_2/Ar flow (30 mL min^{-1}). The catalyst morphology and elemental distribution were examined by scanning electron microscopy with energy-dispersive X-ray spectroscopy (SEM-EDS) on a ZEISS Sigma 300 microscope (Germany).

$$D = \frac{K \times 1}{\beta \times \mathrm{COS}\theta} \quad (6)$$

where, D = crystallite size (nm); K = 0.9 (Scherrer constant); λ = 0.15406 nm (wavelength of X-ray sources); β = FWHM (radians); θ = Peak position (radians).

Results and discussion

Catalyst characterization

Figure 1a reveals a fundamental reconstruction of the catalyst's crystalline structure. Sharp diffraction peaks at 25.8°, 31.8°, 32.9°, 39.6°, 46.6°, and 49.5°, perfectly matching hydroxyapatite (HAP)[39], confirm its highly crystalline inorganic framework. After treatment with 30% phosphoric acid, the characteristic HAP peaks of 30P@FC significantly weaken or even partially disappear, transforming the pattern into a broad, amorphous diffuse halo. This indicated that the phosphoric acid treatment disrupted the long-range ordered crystal structure of HAP, generating an amorphous calcium phosphate composite phase[40,41]. Following iron loading, new broadened diffraction peaks appear at 33.2°, 35.6°, 38.2°, and 54.7° in the 20Fe-30P@FC pattern, which are attributed to nanocrystalline α-Fe_2O_3[42]. The low crystallinity of these peaks suggests a strong interaction between the iron species and the amorphous support. Notably, the significant peak broadening allowed for an estimation of an average crystallite size of approximately 0.83 nm using the Scherrer equation. This indicated that the iron species were highly dispersed on the modified support at the nanoscale. Combined with the observed Fe-O-P bonding signals in Fig. 2, these results collectively confirm the successful construction of an active structure consisting of nano-sized α-Fe_2O_3 intimately composited with the phosphorylated amorphous support.

The textural properties of the catalysts were investigated by N_2 adsorption-desorption analysis, with the results presented in Fig. 1b–d and Table 1. The isotherms for FC, 30P@FC, and 20Fe-30P@FC all exhibit Type IV profiles with H3-type hysteresis loops. As seen in Fig. 1b–d, the relative pressure (P/P_0) at which the adsorbed volume increases sharply shifts to higher values upon further

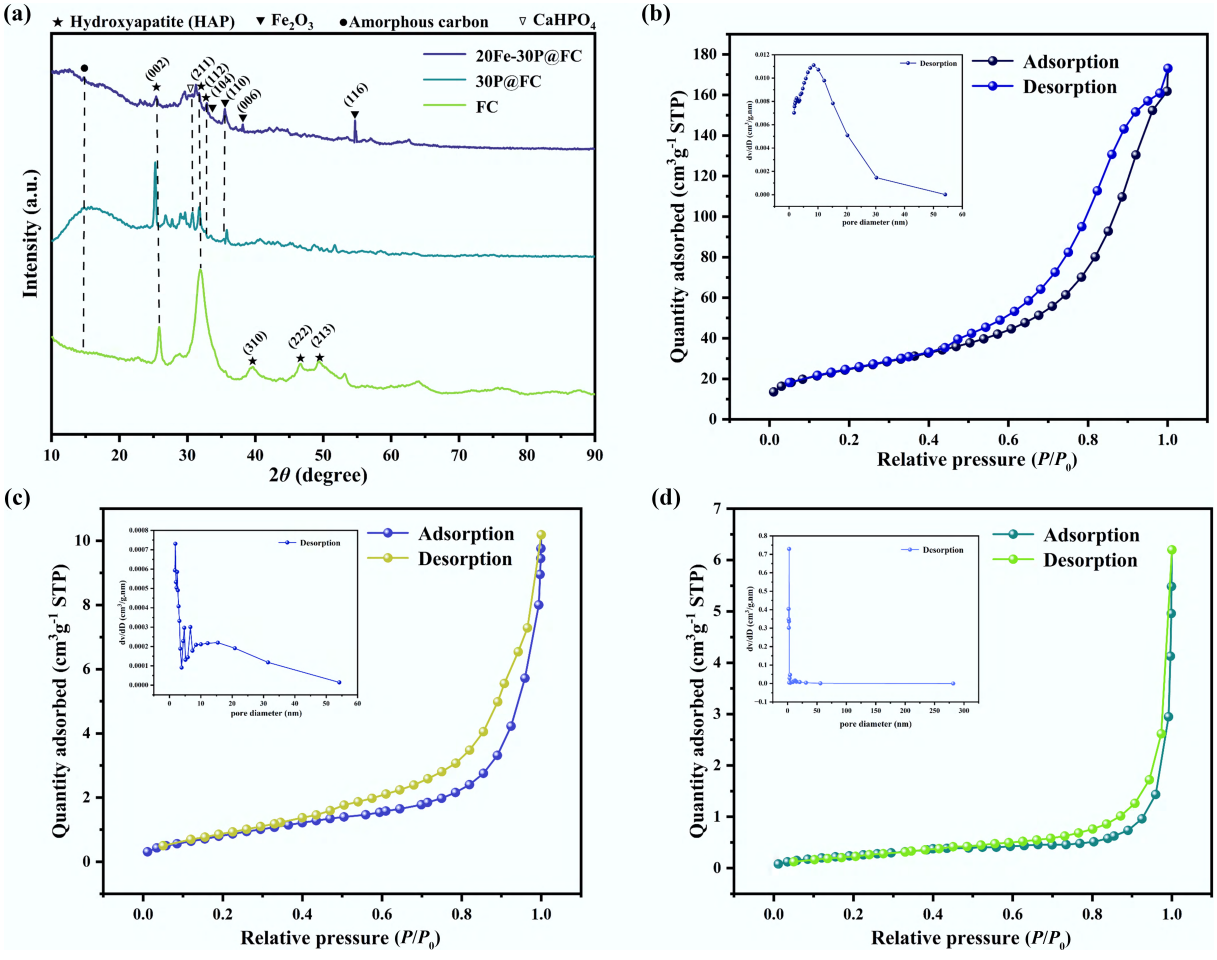

Fig. 1 (**a**) X-ray diffraction patterns of FC, 30P@FC, and 20Fe-30P@FC catalysts. (**b**)–(**d**) N_2-TPD curves of FC, 30P@FC, and 20Fe-30P@FC catalysts, respectively.

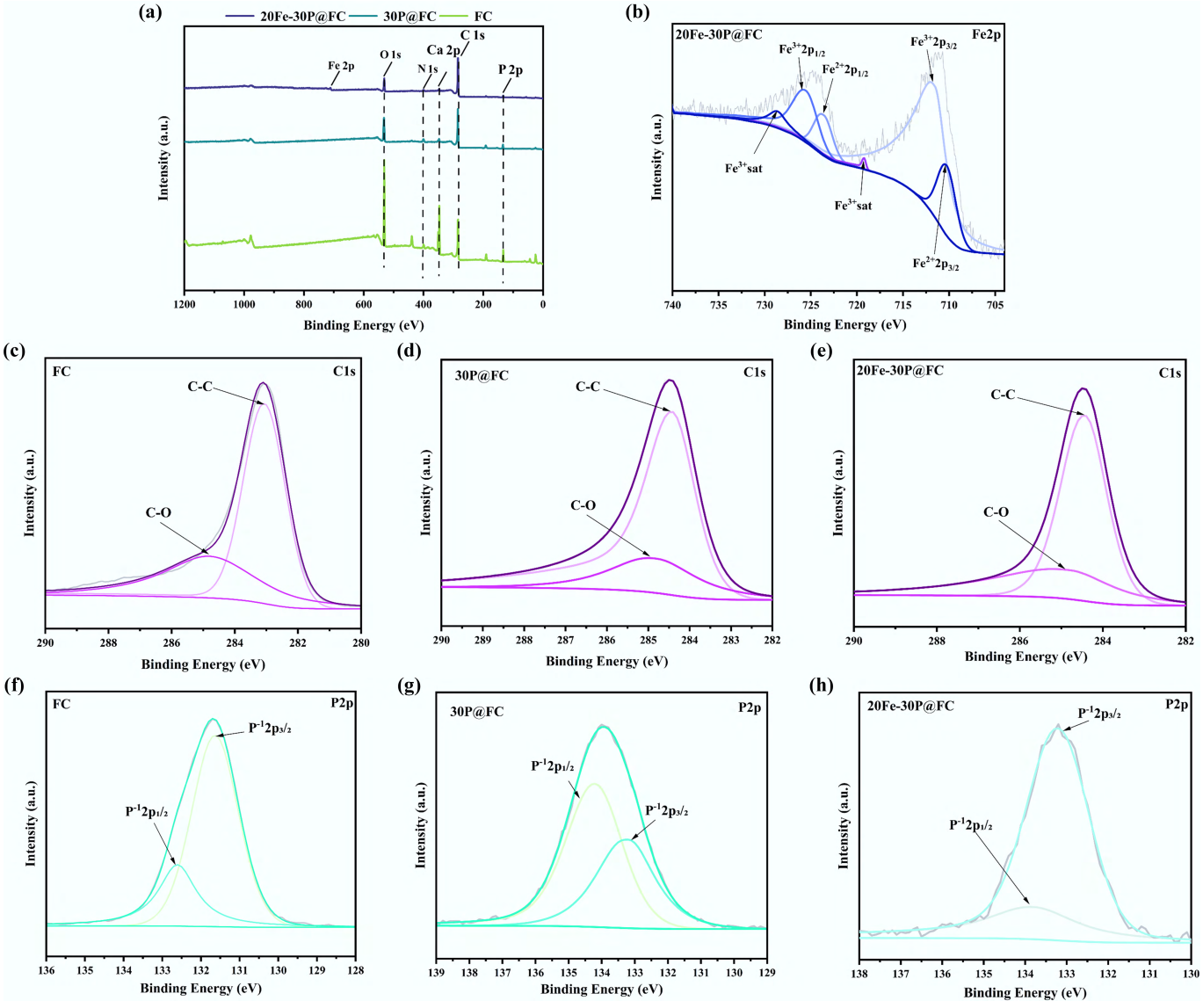

Fig. 2 (**a**) XPS results for FC, 30P@FC, 20Fe-30P@FC XPS measurements. (**b**) Fe2p of 20Fe-30P@FC. (**c**) C1s of FC. (**d**) C1s of 30P@FC. (**e**) C1s of 20Fe-30P@FC. (**f**) P2p of FC. (**g**) P2p of 30P@FC. (**h**) P2p of 20Fe-30P@FC catalysts.

treatment, suggesting the development of more irregular pore structures[43,44]. The specific surface area plummets from 88.73 $m^2 g^{-1}$ for FC to 0.98 $m^2 g^{-1}$ for 20Fe-30P@FC, with the micropore volume nearly vanishing. This provides direct evidence that the phosphoric acid treatment and subsequent iron loading processes cause severe pore blockage and structural densification. Thermogravimetric (TG) analysis further corroborates this observation (Supplementary Fig. S3). The weight loss of FC in the low-temperature region (< 400 °C) is primarily attributed to the decomposition of amorphous carbon and residual organics. In contrast, the TG curves of 30P@FC and 20Fe-30P@FC demonstrate higher thermal stability. A distinct weight loss plateau observed around 600 °C is likely associated with the further condensation of calcium phosphate salts or Fe-O-P species, indicating the formation of more stable composite phases.

Table 1 Structural properties of catalysts

Sample number	FC	30P@FC	20Fe-30P@FC
Fe metal content	0.007%	0.012%	17.251%
P metal content	11.076%	13.309%	6.499%
Ca metal content	24.232%	9.413%	4.800%
BET specific area ($m^2 g^{-1}$)	88.733	3.291	0.982
Micropore volume ($cm^3 g^{-1}$)	22.698	0.182	0.212
Micropore area ($cm^3 g^{-1}$)	0.125459	0.000114	0.000071
Average size (nm)	11.283	18.353	34.564
Hole size (nm)	1.165	12.892	0.827

To further elucidate the nature of interactions between the fish bone-derived catalyst matrix and the introduced P and/or Fe species, X-ray photoelectron spectroscopy (XPS) analysis was conducted. Figure 2 displays the survey spectra, C1s, P2p, and Fe2p core-level spectra for the FC, 30P@FC, and 20Fe-30P@FC catalysts. The Ca2p spectrum (not shown) exhibited typical features characteristic of hydroxyapatite. As shown in Fig. 2b, the C 1s spectra of all fish bone-based catalysts can be deconvoluted into two component peaks at binding energies of approximately 284.8 and 287.4 eV. The first peak is characteristic of C-C bonds, originating from the

https://doi.org/10.48130/scm-0026-0021

bulk carbon skeleton within the bone char[45]. The second peak corresponds to C-O bonds, attributable to residual organic C-O functionalities[46]. After phosphoric acid modification, a strong peak emerges at 134.2 eV in the P 2p spectrum of 30P@FC, which is assigned to P-O-H/P=O species, confirming the successful introduction of acidic phosphate groups[47]. Following iron loading, the Fe $2p_{3/2}$ core-level spectrum of 20Fe-30P@FC (Fig. 2d) was carefully analyzed. The peak is located at a binding energy of approximately 711.5 eV, which is characteristic of Fe^{3+} species[48]. To quantify the electronic perturbation induced by the support, we compared this value to that of a reference pure Fe_2O_3 sample, which exhibits its Fe $2p_{3/2}$ peak at approximately 710.8 eV under identical instrument conditions. The observed positive shift of approximately 0.7 eV for 20Fe-30P@FC indicates a decrease in the electron density around the iron nuclei. Concurrently, the P 2p spectrum of 20Fe-30P@FC shifts towards a lower binding energy (by approximately 0.3–0.5 eV) compared to that of 30P@FC. These opposite and complementary shifts in binding energy provide strong evidence for electron transfer from the Fe species to the adjacent phosphate groups through an Fe-O-P linkage. This strong electronic interaction modulates the electron density of the iron species and is key to creating a unique catalytic interface. Inductively Coupled Plasma Optical Emission Spectroscopy (ICP-OES) further corroborated these findings (elemental contents detailed in Table 1). FC contains high levels of calcium (24.2%) and phosphorus (11.1%). After phosphoric acid treatment, the calcium content in 30P@FC sharply decreases to 9.4%, while the phosphorus content increases to 13.3%, directly reflecting the leaching of Ca from HAP and the introduction of P. The 20Fe-30P@FC catalyst achieved a high iron loading of 17.3%, with a concomitant further reduction in calcium and phosphorus content, aligning with the design strategy for the composite catalyst.

Supplementary Fig. S4 comparatively presents the Fourier Transform Infrared (FT-IR) spectra of the FC, 30P@FC, and 20Fe-30P@FC catalysts, providing vibrational spectroscopic evidence for the structural evolution and the formation of Fe-O-P interfacial bonding. In the pristine FC sample, a broad absorption band around 3,411 cm^{-1} is attributed to the O-H stretching vibration of structural hydroxyl groups within the hydroxyapatite (HAP) lattice. After modification (30P@FC), the intensity of this O-H band significantly diminishes, indicating the consumption of surface hydroxyl groups during chemical treatment, which directly confirms effective chemical reactions between the HAP framework and the modifying agent. More pronounced changes are observed in the phosphate-related vibration regions. Compared to pristine FC, the modified samples exhibit new, strong absorption bands at approximately 1,247 and 1,076 cm^{-1}, assigned to the stretching vibrations of the P=O double bond and P-O-C/P-O single bonds, respectively.

The emergence of these new bands provides definitive evidence for the successful chemical incorporation of phosphate groups onto the catalyst framework, extending beyond the inherent phosphate species of the original HAP structure. The absorption bands at 962 and 1,105 cm^{-1} correspond to the symmetric (ν_1) and asymmetric (ν_3) stretching vibrations of the phosphate (PO_4^{3-}) tetrahedron, which are inherent vibrational modes of the HAP structural units[49,50] and remain present throughout the modification process. Notably, in the iron-loaded 20Fe-30P@FC sample, the P=O characteristic band (~1,247 cm^{-1}) undergoes a distinct redshift and broadening. This redshift indicates a weakening of the P=O bond strength, which is consistent with an alteration in the electron cloud density surrounding the phosphate groups. Such an alteration is typically induced by the introduction of adjacent metal species that interact chemically with the oxygen atoms of the P=O moiety. Simultaneously, a broad absorption band attributable to Fe-O bond vibrations appears in the lower wavenumber region (typically below 800 cm^{-1}). These systematic spectral changes (the redshift of the P=O band and the concurrent appearance of Fe-O vibrations) collectively indicate that the loaded iron species are not merely physically adsorbed onto the surface but engage in strong chemical interactions with the surface phosphate groups. This interaction alters the electron cloud density and local chemical environment of the P=O bonds and leads to the formation of new Fe-O chemical bonds. The spectral evolution observed across the three samples (FC, 30P@FC, 20Fe-30P@FC) thus traces a clear pathway of structural modification: first, the introduction of phosphate groups onto the HAP-derived matrix, followed by the coordination of iron species through oxygen bridges to form a well-defined Fe-O-P interfacial bonding structure. The formation of this Fe-O-P interface is crucial for tuning the electronic properties of the catalyst. By creating a direct chemical linkage between the iron active species and the phosphate-modified support, this interfacial structure enhances the stability of the active component and establishes a unique catalytic environment that is expected to optimize the acid-metal balance, ultimately contributing to improved catalytic performance.

To systematically investigate the influence of surface acidity on catalytic performance, the acidic properties of the catalysts were analyzed using NH_3-TPD, with the results shown in Fig. 3a and the corresponding acid amount and strength distribution data summarized in Table 1. All samples' TPD profiles exhibit two distinct desorption peaks around 127 and 418 °C, which can be attributed to weak and strong acid sites on the catalyst surface, respectively[51]. After phosphoric acid modification, the acidity of 30P@FC changes significantly: the area of the weak acid peak near 127 °C increases notably, and a new strong acid desorption peak appears at a higher temperature (approximately 534 °C). This change directly stems from the successful introduction of phosphate groups. The P-OH groups contribute abundant Brønsted acid sites, while the phosphorus species themselves may also act as Lewis acid sites, collectively enhancing the surface acidity. Upon further loading of iron species, a key modulation in the acid strength distribution occurs for 20Fe-30P@FC. Compared to 30P@FC, the desorption peak temperature of its strong acid sites does not decrease but instead undergoes a significant 'rightward shift' to higher temperatures. This phenomenon, consistent in its physical origin with the observation of altered strong acid sites, indicates strong chemical interaction between the iron species and the support's phosphate groups (Fe-O-P bonding, as seen in Fig. 2g and Supplementary Fig. S4). This interaction likely modulates the acidity through two mechanisms: first, Fe^{3+} ions may exchange with protons (H^+) in the P-OH groups of the support, partially neutralizing the original Brønsted strong acid centers; second, new Lewis acid centers centered on Fe^{3+} are formed, possessing different acid strengths compared to the original protonic acid centers, thereby altering the adsorption strength and desorption energy barrier of NH_3 on the surface. Concurrently, the uniformly dispersed iron oxide nanoparticles observed in SEM images (Fig. 3c) may physically cover some strong acid sites, further influencing acid site distribution and desorption kinetics. In summary, the synergistic effect of phosphoric acid modification and iron species loading successfully enables effective tuning of the catalyst's surface acid amount, strength, and type. This precise design of acidic properties, particularly the modification of strong acid sites and the introduction of new Lewis acid sites, holds significant theoretical and practical value for optimizing the adsorption, activation, and product

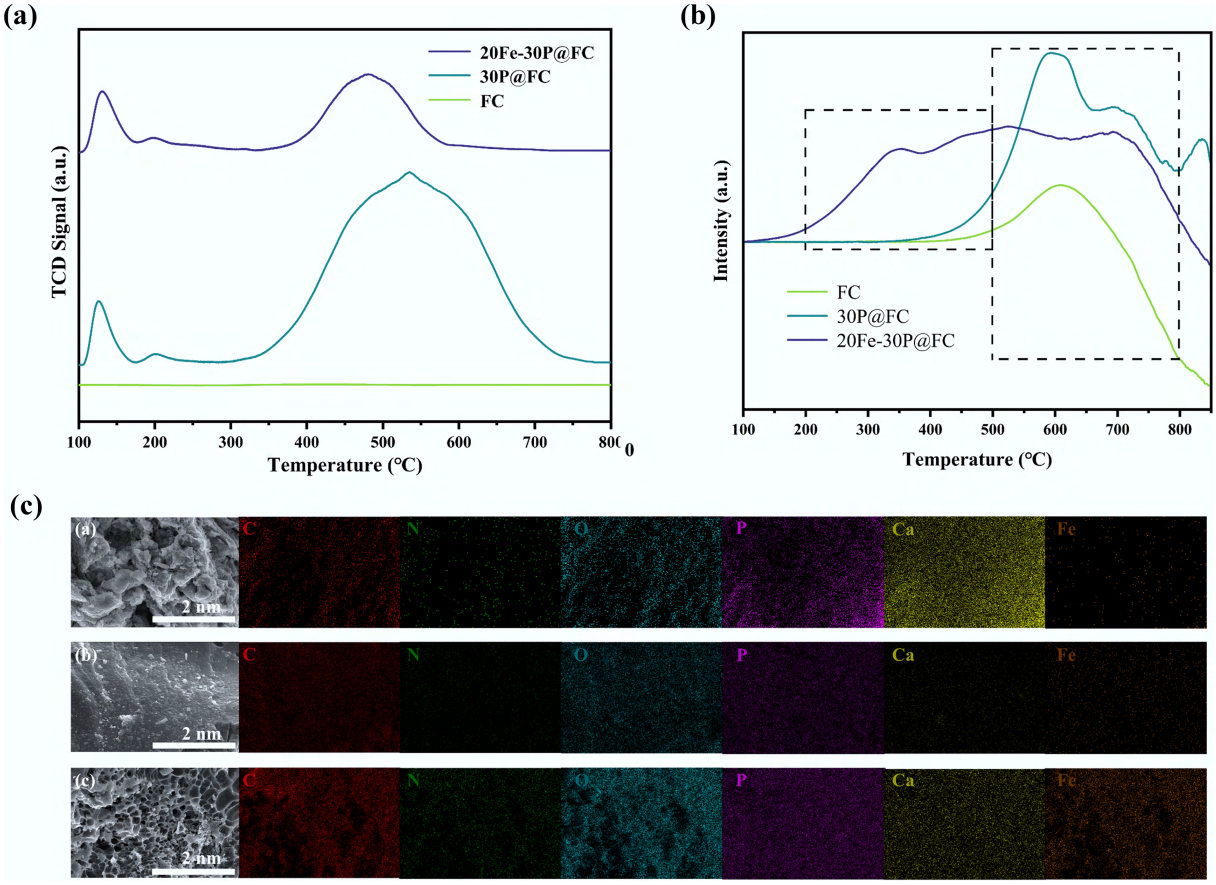

Fig. 3 (**a**) NH_3-TPD spectra of prepared catalysts. (**b**) H_2-TPR spectra of prepared catalysts. (**c**) SEM-EDS spectra of prepared catalysts.

desorption steps of reactant molecules, thereby enhancing the activity and selectivity of the target catalytic reaction.

To investigate the reducibility and distribution of species in the Fe_2O_3 and P-loaded fish bone-based catalysts, H_2-TPR analysis was performed, with the results shown in Fig. 3b. Low-temperature TPR peaks correspond to bulk oxides or species with weak interaction with the support, while high-temperature peaks indicate species that have penetrated the support or formed strong interactions with it[52,53]. FC and 30P@FC show no significant reduction peaks below 600 °C. FC exhibits a strong single reduction peak at 610 °C, which may correspond to the deep transformation of carbonaceous species under a hydrogen atmosphere. For 30P@FC, three stronger reduction peaks appear at 600, 700, and 837 °C. The medium-strength peak at 600 °C is likely associated with the reduction of readily accessible, weakly bound phosphorus-oxygen species in calcium phosphate precursors (e.g., $CaHPO_4$) or their thermally transformed intermediate phases formed during phosphoric acid modification. The strong peak at 700 °C is primarily attributed to the removal of structural oxygen associated with phosphate (PO_4^{3-}) groups within the hydroxyapatite (HAP) framework. The excessive introduction of phosphoric acid may promote the formation of a phosphorus-rich layer on the HAP surface or create lattice defects (e.g., forming pyrophosphate or metaphosphate species). While the P-O bonds in these species are stronger than in pristine HAP, some oxygen atoms can still be removed under strong reducing conditions at this temperature, leading to a significant increase in peak intensity. The extremely high-temperature strong reduction peak at 837 °C indicates the deep reduction of the most stable chemical structures. It likely corresponds to the removal of strongly bound oxygen from highly polymerized or well-crystallized calcium phosphate species (e.g., stable calcium pyrophosphate or phosphate phases highly integrated with the HAP framework) and may even involve the partial reduction of framework phosphate groups. The appearance of this peak demonstrates that phosphoric acid treatment not only modifies the surface but may also induce partial restructuring of the near-surface bulk phase of the support, forming new phases with extremely high thermal stability that are reducible by hydrogen only under intense driving forces. In contrast, 20Fe-30P@FC exhibits two overlapping reduction peaks at 350 and 500 °C. The high-temperature reduction peak (500 °C) is significantly higher than the reduction temperature of pure Fe_2O_3, providing strong evidence for the existence of strong chemical bonding (Fe-O-P) between the iron species and the phosphorylated support. This interaction increases the difficulty of reduction, implying that this interface may maintain a specific oxidation state under reaction conditions to preserve catalytic activity[54]. A broad reduction peak is also observed around 700 °C. The higher reduction temperature for this feature may be due to the more stable nature of the metal species in the catalyst synthesized at high temperatures.

Effect of catalysts on pyrolysis products

The catalytic pyrolysis reaction pathway and product distribution of mulch film plastic exhibit significant differences under the influence of various catalysts. As shown in Fig. 4 and Table 1, a comparative analysis of four systems—non-catalytic pyrolysis, pyrolysis with FC, 30P@FC, and 20Fe-30P@FC catalysts—clarifies the crucial impact of

https://doi.org/10.48130/scm-0026-0021

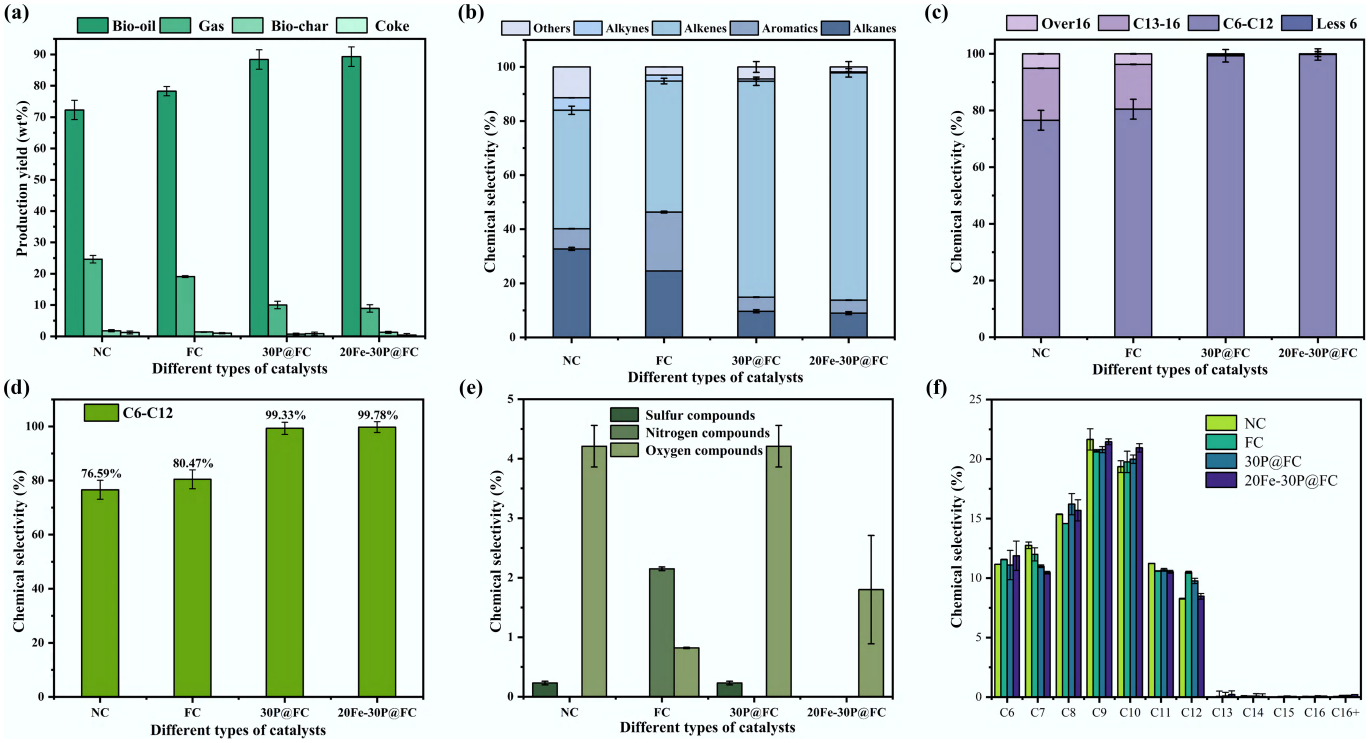

Fig. 4 Yield and composition of bio-oil under different conditions. (**a**) Pyrolysis products. (**b**) Bio-oil composition. (**c**) Distribution of carbon numbers in bio-oil. (**d**) Content of C_6–C_{12} compounds in bio-oil. (**e**) Distribution of other substances in bio-oil. (**f**) Distribution of carbon numbers at optimal acidity.

catalyst structure and composition on the reaction. Non-catalytic pyrolysis, relying primarily on thermal cracking, yields a relatively low bio-oil production (72.3 wt.%) with insufficient olefin selectivity (43.78%), accompanied by the formation of considerable long-chain hydrocarbons and coke. This reflects the indiscriminate nature of pure thermal cracking, which makes selective control of target products challenging[55]. Direct use of the FC catalyst moderately enhances liquid yield and olefin content. The porous carbon framework formed from carbonized fish bone possesses certain adsorption capacity and weak catalytic activity, promoting the cracking of some macromolecules. However, due to its weak acidity and lack of metal active sites, its ability for selective C-C bond scission is limited, resulting in a product still containing a significant proportion of alkanes and C13+ heavy fractions[35]. The 30P@FC catalyst (selected based on acidity screening in Supplementary Fig. S5) demonstrates markedly improved performance. This catalyst successfully introduced abundant Brønsted and Lewis acid sites onto its surface[56,57]. These acid sites effectively promote C-C bond cleavage and stabilize reaction intermediates, thereby increasing olefin selectivity to approximately 80% while simultaneously suppressing coke formation. Nevertheless, this system still shows limitations in facilitating deep dehydrogenation and inhibiting secondary reactions[58]. The 20Fe-30P@FC catalyst (selected based on loading screening in Supplementary Fig. S6) exhibits the best overall performance. The loading of iron species onto the acidic support achieves synergistic catalysis between acid sites and metal active centers. The iron species not only promote dehydrogenation reactions, enhancing selectivity towards olefin formation, but also cooperate with acid sites to modulate hydrogen transfer reactions, effectively suppressing alkane and coke formation. Under this catalytic action, the highest bio-oil yield (89.32 wt.%) is achieved, with olefin selectivity significantly increased to 84.03%. Notably, light olefins (C_6–C_{12}) constitute up to 99.78% of the hydrocarbon products. In summary, the evolution from non-catalytic pyrolysis to the 20Fe-30P@FC catalytic system exemplifies an optimization process in catalyst design: progressing from merely providing a porous structure to introducing acidic functionality, and finally achieving acid-metal bifunctional synergy. The 20Fe-30P@FC catalyst successfully integrates the excellent structural properties of the acid-etched support with the catalytic function of the iron species, providing an efficient and promising solution for the valorization of plastic waste via catalytic pyrolysis.

Effects of pyrolysis temperature

This study employed the 20Fe-30P@FC catalyst, which demonstrated superior performance in promoting the selective formation of olefins in bio-oil. With the catalytic temperature fixed at 350 °C and the catalyst-to-feedstock mass ratio set at 1:2, the influence of pyrolysis temperature (450–650 °C) on the microwave-assisted catalytic pyrolysis of plastic mulch film was systematically investigated. As shown in Fig. 5a, at a pyrolysis temperature of 450 °C, the bio-oil yield was only 69.32 wt.% and the residual coke content was as high as 9.28 wt.%, indicating incomplete pyrolysis reactions under these conditions. As the temperature increased, the bio-oil yield initially rose and then declined, reaching its maximum value of 89.32 wt.% at 550 °C. The composition of the products also changed significantly: the relative content of olefins first increased and then decreased with rising pyrolysis temperature, peaking at 84.03% at 550 °C (Fig. 5b). This trend can be attributed to the endothermic nature of pyrolysis itself; appropriate heating helps provide the necessary energy for the reactions, promoting olefin formation[59]. However, excessively high temperatures accelerate C=C bond cleavage and promote the recombination of carbocations, leading to an increased alkane content[60]. Furthermore, higher pyrolysis temperatures inhibited the formation of C_6–C_{12} hydrocarbons, with their relative content dropping to a minimum of

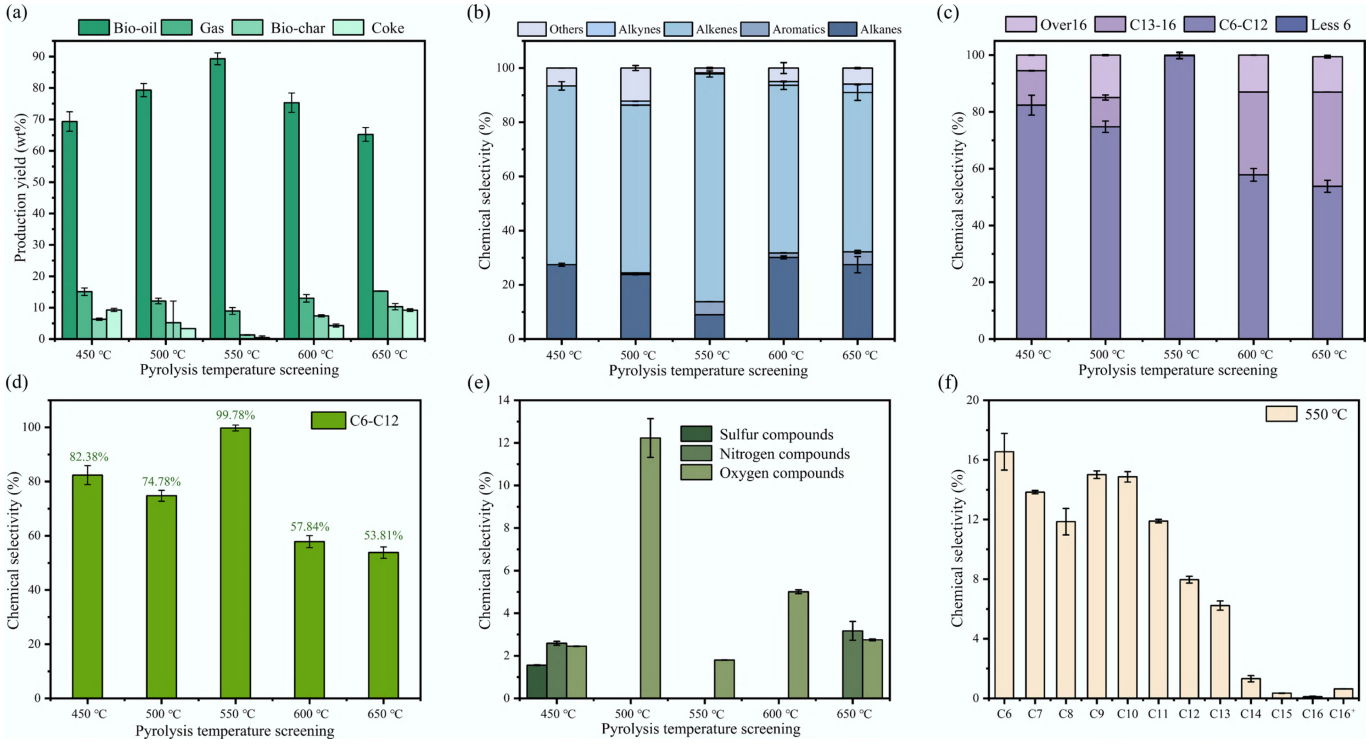

Fig. 5 Effect of pyrolysis temperature on the yield and composition of bio-oil products. (**a**) Pyrolysis products. (**b**) Bio-oil composition. (**c**) Distribution of carbon numbers in bio-oil. (**d**) Content of C_6–C_{12} compounds in bio-oil. (**e**) Distribution of other substances in bio-oil. (**f**) Distribution of carbon numbers at optimal acidity.

53.81% at 650 °C (Fig. 5d). This is likely because elevated temperatures favor the production of long-chain, high-carbon hydrocarbons and promote the secondary cracking of primary pyrolysis vapors, the latter also increasing the yield of non-condensable gases[61]. Considering the bio-oil yield, olefin selectivity, and distribution of light hydrocarbons, 550 °C was identified as the optimal pyrolysis temperature for plastic mulch film using this fish bone-based catalyst. At this temperature, the porous structure created by acid etching and the loaded iron active sites in the catalyst synergistically enhanced mass transfer and the selective cleavage of C-C bonds, thereby enabling the efficient production of high-value-added olefin products.

Effects of catalysis temperature

To determine the optimal catalytic temperature, pyrolysis experiments were conducted using a temperature gradient of 50 °C over a range of 300 to 500 °C. The catalyst used was 20Fe-30P@FC, with a fixed pyrolysis temperature of 550 °C and a catalyst-to-feedstock mass ratio of 1:2. The results, shown in Fig. 6a, indicate that the bio-oil yield initially increased and then decreased with rising catalytic temperature, reaching a maximum of 89.32 wt.% at 350 °C. Concurrently, the yield of non-condensable gases progressively increased. This is attributed to the intensified secondary cracking of primary pyrolysis vapors at higher catalytic temperatures, which promotes the formation of smaller gaseous molecules. Olefin selectivity also peaked at 350 °C (84.03%), declining at both lower and higher temperatures (Fig. 6b). This suggests that an appropriate catalytic temperature facilitates the formation and conversion of reaction intermediates, thereby favoring olefin production, whereas excessively high temperatures can trigger over-cracking and recombination reactions, leading to an increase in by-products such as alkanes and aromatics. The catalytic temperature also significantly influenced the carbon number distribution of olefins (Fig. 6c). When the temperature increased to 350 °C, the relative content of the C_6–C_{12} fraction substantially rose from 90.91% to 99.78%, while the proportions of C13–C16 and C16+ components decreased accordingly. This change indicates that, at a suitable temperature, the synergistic effect between the surface acidity and the iron species on the catalyst promotes the selective cleavage of C-C bonds, favoring the production of more valuable light olefins[62]. However, a further increase in temperature exacerbates alkylation and coking reactions (Fig. 6d), leading to pore blockage and deactivation of the catalyst, which in turn reduces olefin selectivity[63]. In summary, the catalytic temperature presents a crucial trade-off between product distribution and liquid yield by influencing both the reaction pathway and catalyst stability. Based on a comprehensive consideration of bio-oil yield, olefin selectivity, and the yield of low-carbon-number olefins in this study, 350 °C was identified as the optimal catalytic temperature for the pyrolysis of mulch film plastic using this fish bone-based catalyst. This temperature provides sufficient energy to promote C-C bond cleavage and olefin formation while avoiding performance degradation caused by excessive cracking and coking, demonstrating a good synergistic effect between the acid-etched porous support and the loaded iron active sites.

Effect of catalyst-to-feedstock ratio on product distribution

To systematically evaluate the influence of the catalyst-to-feedstock ratio on the reaction pathway and product distribution, this study further investigated the effect of varying the mass ratio of the 20Fe-30P@FC catalyst to mulch film plastic (0:1, 1:3, 1:2, 1:1, 2:1, 3:1) on the microwave-assisted catalytic pyrolysis process under the optimized conditions of a catalytic temperature of 350 °C and a pyrolysis temperature of 550 °C. The results are shown in Fig. 7. As the relative

https://doi.org/10.48130/scm-0026-0021

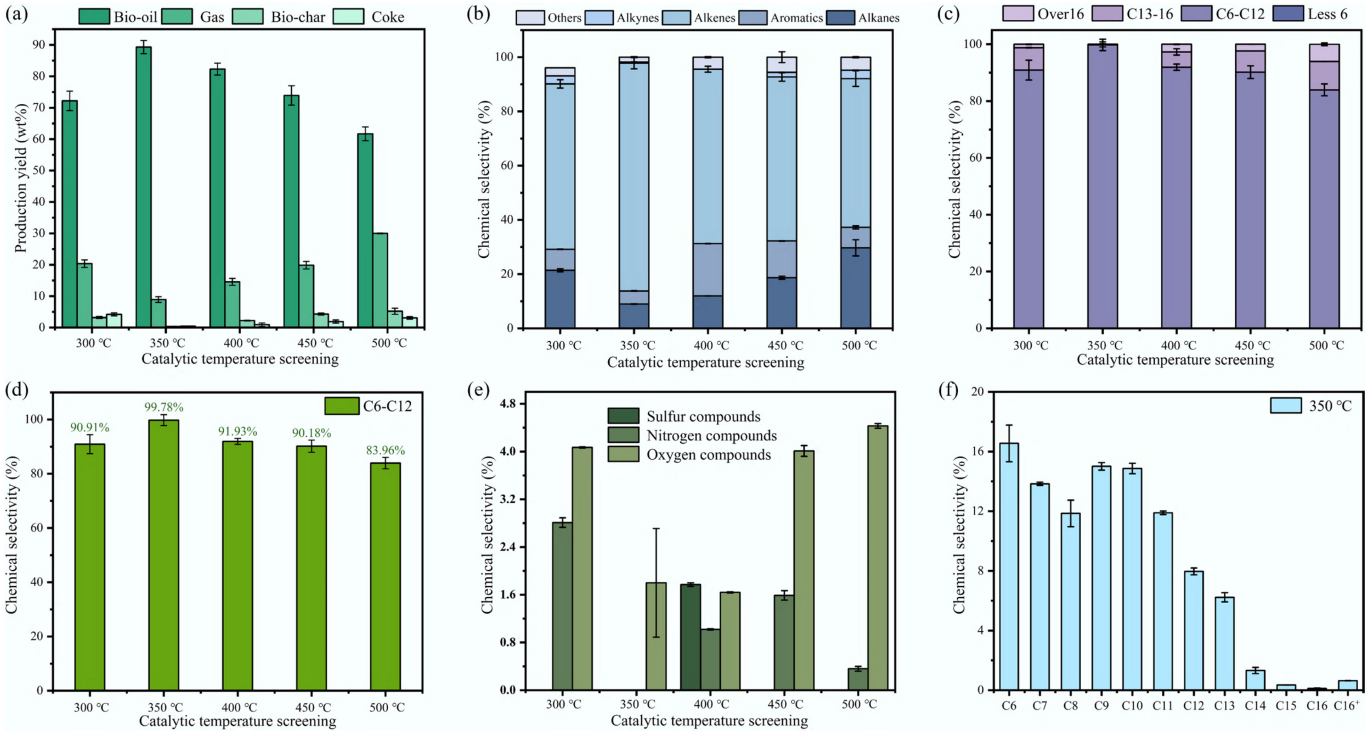

Fig. 6 Effect of catalytic temperature on the yields and composition of bio-oil products. (**a**) Pyrolysis products. (**b**) Bio-oil composition. (**c**) Distribution of carbon numbers in bio-oil. (**d**) Content of C_6–C_{12} compounds in bio-oil. (**e**) Distribution of other substances in bio-oil. (**f**) Distribution of carbon numbers at optimal acidity.

amount of catalyst decreased (i.e., the catalyst/feedstock ratio varied from 0:1 to 3:1), the bio-oil yield exhibited a trend of first increasing and then decreasing (Fig. 7a). The highest liquid yield (89.32 wt.%) was obtained at a ratio of 1:2, indicating that an appropriate number of active sites can effectively promote the conversion of primary cracking vapors into the desired liquid products. At higher ratios (e.g., 1:1), excessive acid sites and iron species may intensify over-cracking and deep dehydrogenation, leading to increased gas yield. Conversely, at lower ratios (e.g., 1:3), insufficient active centers result in inadequate catalytic conversion of the primary pyrolysis products, with partial conversion to coke[64]. The catalyst ratio also exhibited a significant regulatory effect on product selectivity (Fig. 7b). As the ratio decreased from 1:1 to 1:2, olefin selectivity markedly increased from 54.31% to 84.03%. This is because a moderate catalyst loading provides an optimal balance for intermediate adsorption, selective C-C bond scission, and olefin desorption, favoring the olefin formation pathway. However, when the ratio was further reduced to 1:3, olefin selectivity decreased to 59.73%, accompanied by a corresponding increase in alkane content. This is attributed to the reduced probability of radicals contacting active sites under catalyst-deficient conditions, which enhances non-catalytic thermal polymerization and hydrogen transfer reactions, thereby promoting the formation of alkanes and aromatic structures[65]. Analysis of the olefin carbon number distribution further corroborates this mechanism (Fig. 7c). Under the optimal ratio of 1:2, the relative content of C_6–C_{12} light olefins was the highest (99.78%), indicating that the acidic environment and metal active sites provided by the catalyst under these conditions can effectively suppress the formation and re-polymerization of long-chain olefins, promoting their cleavage into the target fraction. Deviations from this optimal ratio resulted in decreased selectivity towards light olefins. In conclusion, the catalyst-to-feedstock ratio is a key parameter for balancing the reaction network. A ratio of 1:2 in this catalytic system achieved the best match between the number of active sites, mass transfer efficiency, and reaction pathway selectivity, ensuring a high bio-oil yield while maximizing the selective production of high-value-added light olefins. This result highlights the practicality and tunability of the developed acid-etched, iron-loaded fish bone-based catalyst for optimizing plastic catalytic pyrolysis processes.

Stability testing of catalysts

To assess the catalyst's stability under practical, continuous operation, five consecutive usage cycles of the 20Fe-30P@FC catalyst were conducted under fixed conditions (pyrolysis temperature: 550 °C, catalytic temperature: 350 °C, catalyst/feedstock mass ratio: 1:2). The evolution of its performance is shown in Fig. 8. With increasing cycle number, the catalyst performance exhibited a regular decline. The bio-oil yield gradually decreased from 89.32 wt.% in the first run to 86.52wt.% in the fifth run (Fig. 8a), while the selectivity towards the target olefins dropped from 84.03% to 82.32% (Fig. 8b). The selectivity for the C_6–C_{12} fraction also decreased from 99.78% to 99.11%. Correspondingly, the yield of non-condensable gases increased from 8.94 wt.% to 10.39 wt.%, the coke yield rose from 0.43 wt.% to 0.87 wt.%, and the selectivity for other by-products increased from 1.8% to 2.78% (Fig. 8e). This trend indicates a continuous weakening of the accessibility of the catalyst's active sites and its ability to selectively control the reaction pathways during cycling, with the reaction gradually shifting towards non-selective thermal cracking. Deactivation is primarily attributed to the progressive deposition of carbonaceous species (coke) on the catalyst surface during the reaction[61]. The coke layer not only physically covers the Fe active centers and acid sites but may also cause partial pore blockage, increasing mass transfer resistance for reactants and products and limiting their contact with internal active

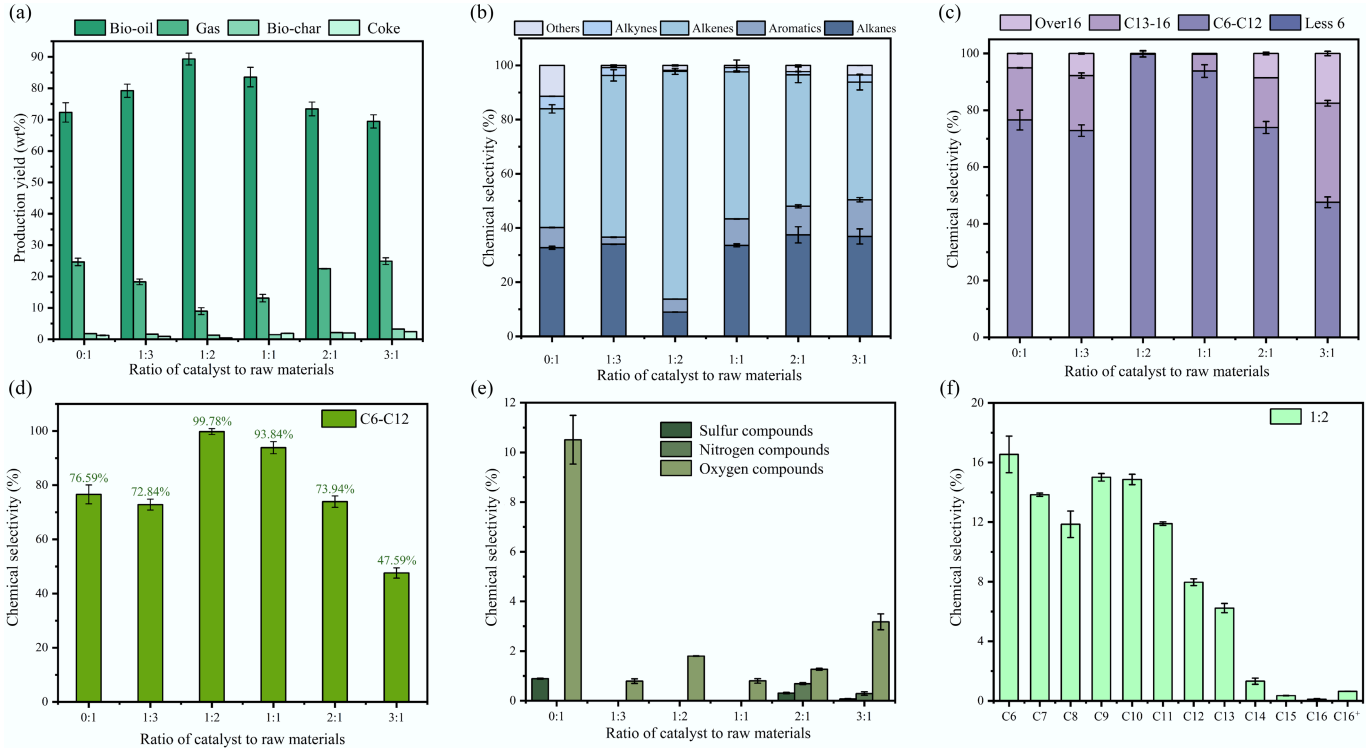

Fig. 7 Effect of catalyst-to-feedstock ratio on the yield and composition of bio-oil products. (**a**) Pyrolysis products. (**b**) Bio-oil composition. (**c**) Distribution of carbon numbers in bio-oil. (**d**) Content of C_6–C_{12} compounds in bio-oil. (**e**) Distribution of other substances in bio-oil. (**f**) Distribution of carbon numbers at optimal acidity.

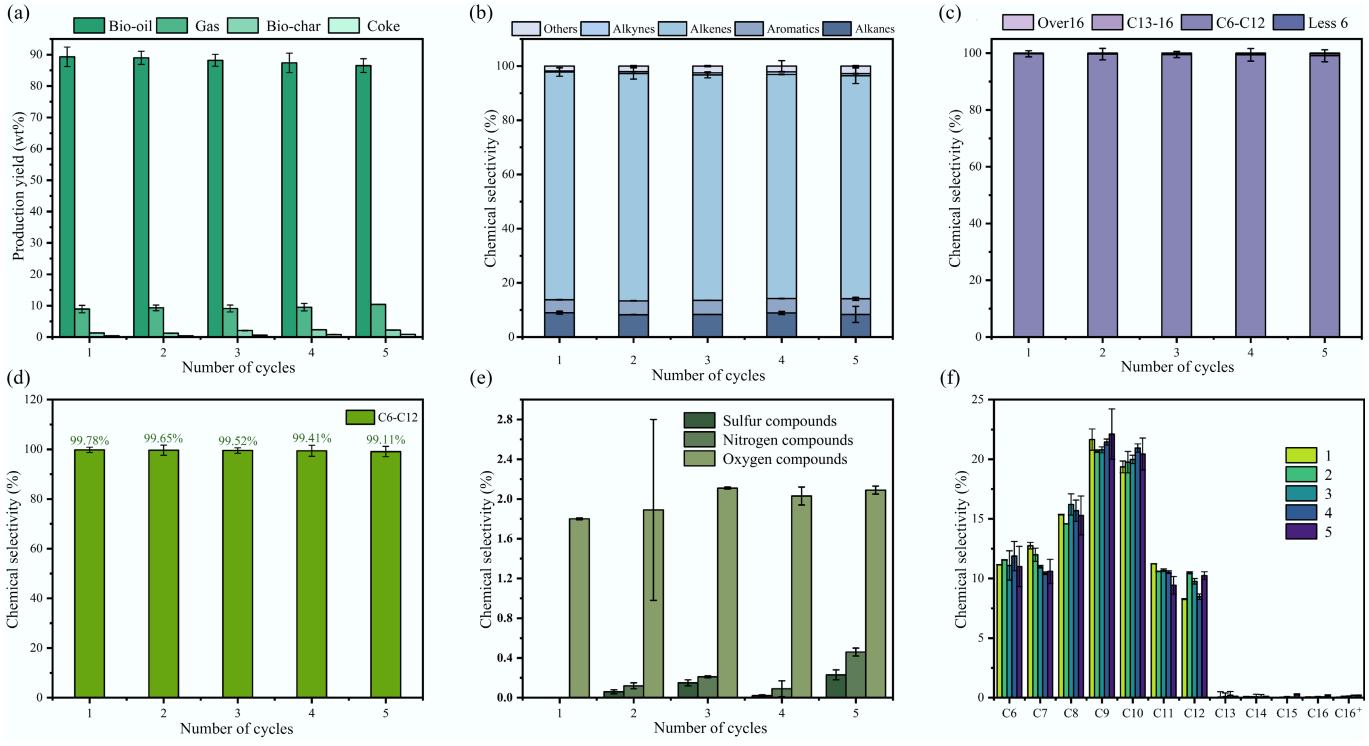

Fig. 8 Yield and composition of fifth-cycle bio-oil. (**a**) Pyrolysis products. (**b**) Bio-oil composition. (**c**) Distribution of carbon numbers in bio-oil. (**d**) Content of C_6–C_{12} compounds in bio-oil. (**e**) Distribution of other substances in bio-oil. (**f**) Distribution of carbon numbers at optimal acidity.

sites. The coverage of acid sites directly impairs the catalyst's ability to activate C-C bonds and stabilize key intermediates, leading to reduced cracking depth and product selectivity[66]. XPS confirmed that Fe exists as electron-deficient Fe^{3+} (Fe $2p_{3/2}$ = 711.5 eV, +0.7 eV shift vs Fe_2O_3), which weakens π-backbonding with olefins and inherently suppresses coke formation. However, over multiple cycles, even this optimized

https://doi.org/10.48130/scm-0026-0021

interface gradually accumulates deposits. The more pronounced decline in olefin selectivity (84.03% to 82.32%) correlates with compromised Fe site function, while the moderate increase in gas yield reflects gradual acid site coverage. NH_3-TPD demonstrated that Fe-O-P formation reconstructs acid sites (strong acid sites shift to higher temperature), creating optimized acidity that resists rapid coking, explaining why the catalyst maintains > 82% selectivity even after five cycles. The Fe-O-P structure is fully restorable upon regeneration. Since deactivation is due to reversible coke coverage rather than structural degradation, calcination under nitrogen should remove carbon deposits while preserving the Fe-O-P framework. In summary, the catalyst's remarkable olefin selectivity retention stems from its unique Fe-O-P interfacial design. It also points out that coking as the key factor limits the long-term stability of this class of biomass-derived catalysts, pointing the way toward enhancing their industrial application potential through surface modification, pore structure optimization, or the incorporation of anti-coking components.

Catalytic conversion mechanism

In the microwave-assisted catalytic pyrolysis system for agricultural plastic films, the structural and functional evolution of catalysts plays a decisive role in directing the preparation of highly selective olefins. As shown in Fig. 9, the FC, 30P@FC, and 20Fe-30P@FC series of catalysts constructed in this study clearly demonstrate an evolutionary pathway from reliance on physical structure to enhanced acidic functionality, and ultimately to the realization of synergistic metal-acid catalysis. The bulk heating and selective 'hot spot' effects of the microwave field, combined with the characteristics of catalysts at different stages, jointly regulate the reaction process and product distribution.

The initial fishbone-based catalyst (FC) features a porous (primarily mesoporous) hydroxyapatite/carbon composite framework. Its large specific surface area and surface weak acid/base sites provide initial adsorption and thermal cracking sites for plastic macromolecules. However, its catalytic activity is low, and cracking is highly random, resulting in limited bio-oil yield and olefin selectivity, along with a broad carbon number distribution[67].

The phosphate-modified 30P@FC catalyst successfully introduced abundant Brønsted and Lewis acid sites on its surface (confirmed by Fig. 3a and Supplementary Fig. S4). Under microwave conditions, these strong acid sites functioned as localized active centers, shifting the catalytic mechanism to an acid-dominated positive carbocation cracking pathway. This pathway significantly promotes selective C-C bond cleavage, enhancing olefin yield and bio-oil quality (olefin selectivity 79.82%, C_6–C_{12} selectivity 99.33%). However, the sole presence of strong acidic functionality also readily induces excessive cracking, aromatization, and coking[68]. Concurrently, partial densification of the framework induced by phosphoric acid treatment (SEM) may partially restrict mass transfer.

The key breakthrough lies in the development of the 20Fe-30P@FC catalyst. Strong interactions between iron loading and the phosphoric acid-modified carrier form a stable Fe-O-P interfacial structure (confirmed by Fig. 2, Supplementary Fig. S4, and Fig. 3c). This chemically bonded interface establishes a carbocation-mediated dehydrogenation mechanism rather than a radical pathway, supported by the high selectivity toward C_6–C_{12} olefins (> 99%) with narrow distribution and the absence of radical-coupling byproducts. The P-modified acid sites provide Brønsted acidity that protonates hydrocarbon chains to generate carbocation intermediates, while Fe sites facilitate subsequent dehydrogenation. C-C bond cleavage is primarily executed by P-modified acid sites via carbocation chemistry. The strong Brønsted acid sites (NH_3-TPD confirmed) protonate C=C bonds or abstract hydride from alkanes, generating carbocation intermediates that undergo β-scission. Upon Fe loading, these acid sites are not eliminated but electronically modulated: the rightward shift of the strong acid peak to higher temperature (Fig. 3a) indicates optimized acid strength, sufficient for controlled C-C activation but moderated to prevent excessive cracking. Hydrogen transfer and olefin formation are primarily executed by Fe sites but critically influenced by electronic effects from the Fe-O-P linkage. XPS reveals that Fe exists as electron-deficient Fe^{3+} (Fe $2p_{3/2}$ = 711.5 eV, +0.7 eV shift vs. Fe_2O_3) due to directional electron transfer from Fe to P via the oxygen bridge (P 2p −0.4 eV shift). This electron-deficient state weakens π-backbonding

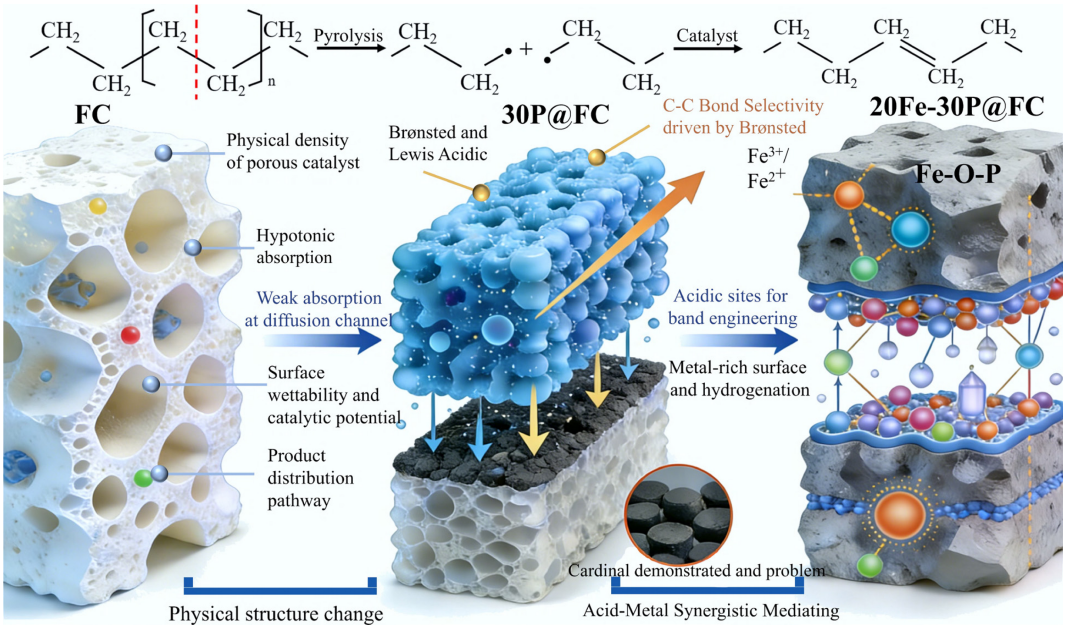

Fig. 9 Catalytic pyrolysis of ground film plastic mechanisms using fishbone-based catalysts.

with olefin intermediates, preventing their strong adsorption and facilitating rapid olefin desorption. Simultaneously, the Fe^{3+}/Fe^{2+} redox pair (as verified by H_2-TPR) actively accepts hydride ions from carbocation intermediates to form olefins. Olefin stabilization results from the intimate proximity ensured by Fe-O-P chemical bonding. Acid sites generate carbocation intermediates, while adjacent Fe sites accept hydride ions to form olefins. The electron-deficient character of Fe ensures quick olefin release before secondary reactions (aromatization, coking) occur. FT-IR confirms this intimacy through P=O redshift (indicating P gains electron density) and Fe-O vibration emergence below 800 cm^{-1}. In the microwave system, Fe-based active sites generate efficient localized heating at the interface, significantly promoting C-H bond activation and dehydrogenation steps. The Fe^{3+}/Fe^{2+} redox pair synergizes with modulated adjacent acid sites, achieving metal-acid bifunctional coordination: Fe sites drive dehydrogenation to generate olefin intermediates, while synergistic acid sites precisely regulate cracking depth and isomerization while promoting surface hydrogen transfer. This synergistic mechanism concentrates product selectivity toward high-value C_6–C_{12} light olefins (99.78% selectivity) while significantly suppressing carbon deposit precursor formation through efficient hydrogen transfer (0.43% coke yield).

Conclusions

This study systematically evaluated the effects of phosphoric acid modification and iron loading on the microwave-assisted catalytic pyrolysis performance of 20Fe–30P@FC at a pyrolysis temperature of 550 °C, a catalytic temperature of 350 °C, and a catalyst-to-feedstock ratio of 1:2. Under these optimized conditions, 20Fe–30P@FC achieved a maximum bio-oil yield of 89.32 wt.%, with the product dominated by olefins (84.03%), accompanied by minor fractions of alkanes (8.98%) and aromatics (4.80%). Notably, the alkyne content remained extremely low (0.29%), indicating a strong synergistic interaction between acidic sites and iron species. Regeneration tests further demonstrated stable catalytic activity and oil yield over multiple cycles, confirming the robustness of the catalyst.

Compared with Fe-only catalysts, phosphoric acid pretreatment significantly enhanced performance, which is attributed to the formation of Fe-O-P interfacial structures that modulate the electronic properties of iron species. This interaction promotes a hydrogenation–decyclization pathway, suppressing polycyclic aromatic hydrocarbon precursors and partially converting aromatic intermediates into light olefins, thereby improving product selectivity. Overall, the fish bone–derived acid–metal bifunctional catalyst enables efficient and selective conversion of agricultural plastic film waste, offering a cost-effective route for plastic valorization and highlighting the potential of biomass-derived catalysts in high-value solid waste conversion.

Supplementary information

It accompanies this paper at: https://doi.org/10.48130/scm-0026-0021.

Author contributions

The authors confirm their contributions to the paper as follows: all authors: conceptualization, design, writing-review and editing; Zhang Yue, Lan Xiaoyan, Chen Xun, Gan Lu, Zhang Jian, Dai Leilei, Duan Dengle: Material preparation, data collection and analysis; Zhang Yue: writing-original manuscript. All authors reviewed the results and approved the final version of the manuscript.

Data availability

The datasets used or analyzed during the current study are available from the corresponding author upon reasonable request.

Acknowledgments

We gratefully acknowledge the Analysis and Testing Center of Shihezi University, which provided analytical and testing support for this experiment.

Funding

This work was supported by CAS Key Laboratory of Renewable Energy (No. E129kf0401), the financial support from the Xinjiang Construction Corps Guiding Program (KX009303), Shihezi University High-level Talent Project (2022ZD060), Tianchi Talent Young Doctor Project (CZ0023406).

Declarations

Competing interests

The authors declare that they have no conflict of interest.

Author details

[1]School of Food Science and Technology, Jiangnan University, 1800 Lihu Avenue, Wuxi, Jiangsu 214122, China; [2]Key Laboratory of Renewable Energy and Guangzhou Institute of Energy Conversion, Chinese Academy of Sciences, Guangzhou 510640, China; [3]Key Laboratory of Agricultural Product Processing and Quality Control of Specialty (Co-construction by Ministry and Province), School of Food Science and Technology, Shihezi University, Shihezi, Xinjiang 832003, China; [4]Key Laboratory for Food Nutrition and Safety Control of Xinjiang Production and Construction Corps, School of Food Science and Technology, Shihezi University, Shihezi, Xinjiang 832003, China; [5]Guangdong Provincial Key Laboratory of Lingnan Specialty Food Science and Technology, Zhongkai University of Agriculture and Engineering, Guangzhou 510225, China; [6]Key Laboratory of Energy Thermal Conversion and Control, School of Energy and Environment, Southeast University, Nanjing 211189, China; [7]State Key Laboratory of Food Science and Technology, Nanchang University, Nanchang 330047, China; [8]Center for Biorefining and Department of Bioproducts and Biosystems Engineering, University of Minnesota, 1390 Eckles Ave., St. Paul, MN 55108, USA; [9]Jiangsu Key Laboratory of Micro and Nano Heat Fluid Flow Technology and Energy Application, School of Physical Science and Technology, Suzhou University of Science and Technology, Suzhou 215009, China; [10]Department of Biological Systems Engineering, Washington State University, Richland, WA 99354, USA

References

[1] Xiong XB, Zhao ZY, Wang PY, Lu XY, Zhu Y, et al. 2026. Conservation mulching with plastic film in maize field of arid irrigation region: agronomic performance, economic, and environmental effects. *Field Crops Research* 337:110283

[2] Quintana MA, Garcia-Garcia G, Blazquez G, Martín-Lara MA, Calero M, et al. 2026. Pyrolysis as the gateway thermochemical route for plastic-to-hydrogen-rich gas valorization. *Journal of Analytical and Applied Pyrolysis* 193:107480

[3] Wang B, Sloan J, Lee H, Jung M, Tang YJ, et al. 2026. Tillage changes transport and fate of microplastics in the agricultural environment. *Agriculture, Ecosystems & Environment* 399:110145

[4] Xiao H, Li S, Shi Z, Cui C, Xia S, et al. 2023. Plasma-catalytic pyrolysis of polypropylene for hydrogen and carbon nanotubes: understanding the influence of plasma on volatiles. *Applied Energy* 351:121848
[5] Dai L, Zhao H, Zhou N, Cobb K, Chen P, et al. 2023. Catalytic microwave-assisted pyrolysis of plastic waste to produce naphtha for a circular economy. *Resources, Conservation and Recycling* 198:107154
[6] Fu W, Zhang Y, Liu Z, Zhao W, Liu W, et al. 2025. Microwave-assisted catalytic pyrolysis of polypropylene for aviation fuel production with Fe/Ni catalysts: a comparison with electrical catalytic pyrolysis. *Energy Conversion and Management* 340:119993
[7] Anuar Sharuddin SD, Abnisa F, Wan Daud WMA, Aroua MK. 2016. A review on pyrolysis of plastic wastes. *Energy Conversion and Management* 115:308–326
[8] Keyhani S, Prussi M, Chiaramonti D. 2025. Review on marine plastic pyrolysis oil: turning pollution into a maritime fuel. *Applied Energy* 401:126759
[9] Hegedüs B, Dinh T, Nagy G, Muránszky G, Dobó Z. 2026. Temperature-dependent investigation of pyrolysis products from PP and LDPE for Gasoline-like fuel applications. *Waste Management* 210:115262
[10] Zhang Y, Yang J, Yu P, Ruan R, Dai L, et al. 2025. Catalytic co-pyrolysis of cotton stalks and ground film plastic using fishbone-based metal catalysts: enhanced production of olefins and aromatics. *Chemical Engineering Journal* 521:166274
[11] Liu J, Li Y, Deng W, Wu Y, Chen D, et al. 2025. Study on a potential bone char catalyst for high efficiency catalytic pyrolysis of polypropylene plastic. *Fuel* 381:133625
[12] Pagán J, Ibarz A, Falguera V, Benítez R. 2013. Enzymatic hydrolysis kinetics and nitrogen recovery in the protein hydrolysate production from pig bones. *Journal of Food Engineering* 119:655–659
[13] Alkurdi SSA, Al-Juboori RA, Bundschuh J, Hamawand I. 2019. Bone char as a green sorbent for removing health threatening fluoride from drinking water. *Environment International* 127:704–719
[14] Chotiratanasak J, Promdee K, Vitidsant T, Khemkhao M. 2025. Effect of acid catalysts on yield and selectivity of plastics waste pyrolysis from municipal solid waste in Samui Island, Thailand. *Results in Engineering* 28:107770
[15] Armenise S, Luing WS, Romero Vázquez MA, Pérez-Guevara E, Prieto C, et al. 2025. Tailoring catalyst acidity and hierarchical pore structure for enhanced BTX yields in plastic waste pyrolysis. *Journal of Environmental Chemical Engineering* 13:119493
[16] Nazarloo NH, Shirvanimoghaddam K, Zabihi O, Naebe M. 2024. Catalytic pyrolysis of plastic waste using activated carbon from cotton waste. *Journal of Analytical and Applied Pyrolysis* 182:106692
[17] López A, de Marco I, Caballero BM, Laresgoiti MF, Adrados A, et al. 2011. Catalytic pyrolysis of plastic wastes with two different types of catalysts: ZSM-5 zeolite and Red Mud. *Applied Catalysis B: Environmental* 104:211–219
[18] Miandad R, Barakat MA, Aburiazaiza AS, Rehan M, Ismail IMI, et al. 2017. Effect of plastic waste types on pyrolysis liquid oil. *International Biodeterioration & Biodegradation* 119:239–252
[19] Syamsiro M, Saptoadi H, Norsujianto T, Noviasri P, Cheng S, et al. 2014. Fuel oil production from municipal plastic wastes in sequential pyrolysis and catalytic reforming reactors. *Energy Procedia* 47:180–188
[20] Liu J, Li Y, Zhang X, Yang Z, Liu X, et al. 2026. A highly efficient and recyclable bone char for catalytic pyrolysis of polypropylene. *Journal of Environmental Management* 397:128174
[21] Rodríguez S, Trueba D, Escribano M, Arandes JM, Palos R, et al. 2025. Six-lump kinetic model for plastic pyrolysis oil (PPO) and vacuum gasoil (VGO) blend hydroprocessing considering selective catalyst deactivation. *Catalysis Today* 457:115341
[22] Dong CD, Huang CP, Chen CW, Hung CM. 2024. Advanced sustainable processes via functionalized Fe–N Co-doped fishbone biochar for the remediation of plasticizer di-(2-ethylhexyl) phthalate-contaminated marine sediment. *Environmental Pollution* 348:123861
[23] Wang Y, Wang CH. 2025. Sustainable production of carbon nanotubes from plastic pyrolysis using Ni- and Fe-biochar catalysts synthesized via hydrothermal treatment. *Applied Catalysis B: Environment and Energy* 373:125340
[24] Shu D, Gan L, Zhang Y, Sun X, Tan C, et al. 2024. A solid acid derived from fishbone catalyzes the hydrolysis of cellulose into nanocellulose. *International Journal of Biological Macromolecules* 275:133903
[25] Liu Z, Liu T, Zhao W, Zhang Y, Liu W. 2026. Rich hydrogen syngas production from microwave-assisted catalytic pyrolysis of polypropylene plastic particles. *Journal of Analytical and Applied Pyrolysis* 195:107628
[26] Qiu T, Xie K, Liu C, Ahmad F, Zhao W, et al. 2025. Microwave-assisted pyrolysis for advanced sustainable carbon materials. *Sustainable Carbon Materials* 1:e011
[27] Cui L, Zhang Y, Shi C, Zhao W, Li B. 2024. Describing the microwave heating performances of the main constitutes of biomass. *Energy* 302:131873
[28] Sun Y, Zhang Q, Clark JH, Graham NJD, Hou D, et al. 2022. Tailoring wood waste biochar as a reusable microwave absorbent for pollutant removal: structure-property-performance relationship and iron-carbon interaction. *Bioresource Technology* 362:127838
[29] Fu W, Zhang Y, Liu Z, Zhao W, Liu W, et al. 2025. Shuai. Kinetic and thermodynamic insights into the catalytic pyrolysis of PP with Fe/Ni catalysts. *Energy* 330:136809
[30] Hassan AA, Smith JD. 2020. Investigation of microwave-assisted transesterification reactor of waste cooking oil. *Renewable Energy* 162:1735–1746
[31] Hussain Z, Khan KM, Perveen S, Hussain K, Voelter W. 2012. The conversion of waste polystyrene into useful hydrocarbons by microwave-metal interaction pyrolysis. *Fuel Processing Technology* 94:145–150
[32] Cui Y, Zhang Y, Cui L, Liu Y, Li B, et al. 2023. Microwave-assisted pyrolysis of polypropylene plastic for liquid oil production. *Journal of Cleaner Production* 411:137303
[33] Ahmad F, Zhang Y, Liu Z, Zhao W, Liu W, et al. 2025. Aromatic enriched oil production via microwave-assisted catalytic co-pyrolysis of baked semen abutilon seeds and waste expanded polystyrene. *Journal of Cleaner Production* 528:146660
[34] Qiu T, Li C, Zhao W, Naz MY, Zhang Y. 2025. Microwave-assisted pyrolysis of biomass: influence of feedstock and pyrolysis parameters on porous biochar properties. *Biomass and Bioenergy* 193:107583
[35] Zhang Y, Xu Y, Tan C, Ruan R, Dai L, et al. 2025. Preparation of highly selective olefins from pyrolyzed ground film plastics catalyzed by fishbone-based catalysts. *Process Safety and Environmental Protection* 201:107565
[36] Arpia AA, Chen WH, Ubando AT, Tabatabaei M, Lam SS, et al. 2021. Catalytic microwave-assisted torrefaction of sugarcane bagasse with calcium oxide optimized via Taguchi approach: product characterization and energy analysis. *Fuel* 305:121543
[37] Fan S, Zhang Y, Cui L, Maqsood T, Nižetić S. 2023. Cleaner production of aviation oil from microwave-assisted pyrolysis of plastic wastes. *Journal of Cleaner Production* 390:136102
[38] Zhou N, Dai L, Lv Y, Li H, Deng W, et al. 2021. Catalytic pyrolysis of plastic wastes in a continuous microwave assisted pyrolysis system for fuel production. *Chemical Engineering Journal* 418:129412
[39] Schwarcz HP, Binkley DM, Luo L, Grandfield K. 2020. A search for apatite crystals in the gap zone of collagen fibrils in bone using dark-field illumination. *Bone* 135:115304
[40] Marrakchi F, Toor SS, Pedersen TH, Rosendahl LA. 2026. Hydrothermal co-liquefaction of rye straw, shellfish, and beef tallow using CaO-MgO-apatite composite catalyst: hybrid models of biomacromolecules under sub-, near, and supercritical conditions for predicting yield and properties of multiphase HTL products. *Chemical Engineering Journal* 527:170589
[41] Sun D, Liao T, Lin H, Sang Y, Liu Y, et al. 2024. Sustainable double-synergistic silver-hydroxyapatite composite catalyst derived from fish bones for efficient disinfection of *Vibrio parahaemolyticus*. *Food Chemistry* 456:139915
[42] Sen SK, Hossain MS, Roy R, Alam MS, Manir MS, et al. 2024. Size-strain distribution analysis from XRD peak profile of (Mg, Fe) Co-doped SnO_2 nanoparticles fabricated using chemical co-precipitation route. *Ceramics International* 50:44038–44055

[43] Qiu T, Cao W, Xie K, Ahmad F, Zhao W, et al. 2025. CO_2 capture performances of H_3PO_4/KOH activated microwave pyrolyzed porous biochar. *Sustainable Carbon Materials* 1:e004

[44] Li C, Shi Y, Zhao QD, Xiong W, Ding Y, et al. 2023. A stable spherical MOF-derived Mnx-Fe_2O_3/C catalysts for low-temperature CO-SCR. *Chemical Engineering Journal* 475:146388

[45] Lewin E, Persson POÅ, Lattemann M, Stüber M, Gorgoi M, et al. 2008. On the origin of a third spectral component of C1s XPS-spectra for nc-TiC/a-C nanocomposite thin films. *Surface and Coatings Technology* 202:3563−3570

[46] Poche T, Wirth W, Jang S. 2024. Chemical structure characteristics of flexible low-k SiCOH thin films etched by inductively coupled plasma-reactive ion etching process using FTIR and XPS spectra analysis. *Microelectronic Engineering* 292:112221

[47] Acheson JG, Robinson L, McKillop S, Wilson S, McIvor MJ, et al. 2021. TOFSIMS and XPS characterisation of strontium in amorphous calcium phosphate sputter deposited coatings. *Materials Characterization* 171:110739

[48] Greczynski G, Hultman L. 2025. Binding energy referencing in X-ray photoelectron spectroscopy. *Nature Reviews Materials* 10:62−78

[49] Ltaief W, Mbarek A, Aboussatar M, El-Ghozzi M, Naïli H, et al. 2025. $LiGd_4(PO_4)_3F_4$: Ln^{3+} (Ln = Eu^{3+} or Tb^{3+}) fluorophosphates as red- or green-emitting phosphors: structural and photoluminescence characterization. *Inorganic Chemistry Communications* 180:115099

[50] Ltaief W, Mbarek A, El-Ghozzi M, Naïli H, Zambon D. 2018. Structural and optical investigations of new fluorophosphates solid solutions $Li_xY_{1-y}Ln_y(PO_4)_{1-x}F_{4x}$ (0< x ≤0 . 4; Ln = Eu, Tb) as phosphors for solid-state lighting. *Journal of Alloys and Compounds* 735:29−42

[51] Liu W, Zhang Y, Wang J, Chen Y, Wang F, et al. 2025. Effect mechanism of coal gangue ash on NH_3 oxidation in NH_3 combustion condition. *Fuel* 385:134140

[52] Jagodzińska K, Jönsson PG, Yang W. 2022. Pyrolysis and in-line catalytic decomposition of excavated landfill waste to produce carbon nanotubes and hydrogen over Fe- and Ni-based catalysts – Investigation of the catalyst type and process temperature. *Chemical Engineering Journal* 446:136808

[53] Yao D, Yang H, Hu Q, Chen Y, Chen H, et al. 2021. Carbon nanotubes from post-consumer waste plastics: investigations into catalyst metal and support material characteristics. *Applied Catalysis B: Environmental* 280:119413

[54] Zhao Y, Deng C, Tang D, Ding L, Zhang Y, et al. 2021. α-Fe_2O_3 as a versatile and efficient oxygen atom transfer catalyst in combination with H_2O as the oxygen source. *Nature Catalysis* 4:684−691

[55] Ronka S. 2014. Properties of novel spherical carbon adsorbents synthesized from phosphorylated polymeric precursors. *Journal of Analytical and Applied Pyrolysis* 110:390−400

[56] Xing W, Wang Z, Zhang K, Xu Y, Pan Y, et al. 2025. Flame-retardant and antibacterial multifunctional cellulose fibers with carbamate esterification and phosphorylation modification. *Industrial Crops and Products* 233:121482

[57] Zhou Y, Yu F, Huang M, Guo Y, Wei J, et al. 2024. The influence mechanism of bitumen components on its macroscopic and microscopic properties: analysis based on polyphosphoric acid modification. *Fuel* 372:132085

[58] Said HA, Ait Bourhim I, Ouarga A, Iraola-Arregui I, Lahcini M, et al. 2023. Sustainable phosphorylated microcrystalline cellulose toward enhanced removal performance of methylene blue. *International Journal of Biological Macromolecules* 225:1107−1118

[59] Apicella B, Cerciello F, Migliaccio R, Oliano MM, Ruoppolo G, et al. 2025. Chemical characterization of liquid products from the pyrolysis of plastic wastes. *Journal of Analytical and Applied Pyrolysis* 190:107153

[60] Zhang X, Wu S, Ge B, Zhou Q, Yan B, et al. 2025. A dual-stage machine learning framework for comprehensive characterization of waste plastic pyrolysis oils. *Journal of Analytical and Applied Pyrolysis* 192:107300

[61] Dhaniswara TK, Juliastuti SR, Mahfud M. 2025. Synergistic effect of Fe-promoted catalyst and low-rank coal absorber in microwave-assisted plastic pyrolysis. *Sustainable Chemistry for Climate Action* 7:100113

[62] Ureel Y, Piña CP, Dunkle MN, Pijcke P, da Costa Magalhaes B, et al. 2025. Detailed analysis of olefins and diolefins in hydrotreated plastic waste pyrolysis oils by GC-VUV. *Waste Management* 202:114828

[63] Li S, Zhang Y, Zhao L, Qin J, Liu H. 2026. Comprehensive evaluation of e-waste plastic pyrolysis technology: research status, technical challenges and prospects. *Journal of Analytical and Applied Pyrolysis* 193:107458

[64] Lin X, Sun Z, Zhuansun X, Li H, Sun C, et al. 2026. Decoupling gas-gas phase interactions in catalytic co-pyrolysis of biomass and plastic over HZSM-5: molecular mechanisms of synergy between oxygenates and olefins. *Renewable Energy* 258:124966

[65] Li Y, Wang W, Yin F, Wang KS. 2025. Threshold temperature pyrolysis of waste plastic and the effect on pyrolysis energy consumption and product distribution. *Thermal Science and Engineering Progress* 67:104105

[66] Muloogi D, Sagala F, Ogene F, Bbosa D, Birungi G. 2025. Potential for optimisation of fuel yield and hydrocarbon distribution from plastic waste pyrolysis using Nanopyroxene catalysts. *Results in Chemistry* 17:102573

[67] Wu J, Tian H, Gu F, Ning H, Huang J, et al. 2026. Preparation and performance evaluation of asphalt modifier from catalytic pyrolysis of waste plastics using Ni modified HZSM-5. *Construction and Building Materials* 506:144938

[68] Chen H, Shan T, Liu S, Liu T, Zhang H. 2026. The effect of plastic type on the product distribution and Cr (VI) removal in the co-pyrolysis of plastics and chromium-containing slag. *Journal of the Energy Institute* 124:102413